Effect of hydroxyapatite concentration and size on morpho-mechanical properties of PLA-based randomly oriented and aligned electrospun nanofibrous mats.

Francesco Lopresti*[1,2], Francesco Carfì Pavia[1,3], Ilenia Vitrano[1], Maïwenn Kersaudy-Kerhoas[2], Valerio Brucato[1], Vincenzo La Carrubba[1]

[1]Department of Engineering, University of Palermo, RU INSTM, Viale delle Scienze, Palermo, Italy
[2]Institute of Biological Chemistry, Biophysics and Bioengineering, Heriot-Watt University, Edinburgh, United Kingdom
[3]ATeN Center, University of Palermo, Viale delle Scienze, Palermo, Italy

*Corresponding: Francesco Lopresti. mail: francesco.lopresti01@unipa.it

Abstract

The growing demand for nanofibrous biocomposites able to provide peculiar properties requires systematic investigations of processing-structure-property relationships. Understanding the morpho-mechanical properties of an electrospun scaffold as a function of the filler features and mat microstructure can aid in designing these systems.

In this work, the reinforcing effect of micrometric and nanometric hydroxyapatite particles in polylactic acid-based electrospun scaffold presenting random and aligned fibers orientation, was evaluated. The particles incorporation was investigated trough Fourier transform infrared spectroscopy in attenuated total reflectance. The morphology of the nanofibers was analyzed through scanning electron microscopy and it was correlated with the viscosity of polymeric solutions studied by rheological measurements. Scaffolds were mechanical characterized with tensile tests in order to find a correlation between the preparation method and the strength of the mats. The influence of hydroxyapatite particles on the crystallinity of the composites was investigated by differential scanning calorimetry. Finally, cell culture assays with pre-osteoblatic cells were conducted on a selected composite scaffold in order to compare the cell proliferation and morphology with that of polylactic acid scaffolds. Based on the results, we can prove that polylactic acid/hydroxyapatite composites can be one of the biomaterials with the greatest potential for bone tissue regeneration.

Keywords: Electrospinning; Aligned fibers; polylactic acid; Hydroxyapatite; pre-osteoblatic cells;

1. Introduction

In tissue engineering (TE), there is a growing demand for functional polymeric nanofiber scaffolds able to provide fibrous matrix networks similar to extracellular matrix (ECM) to support cells and able to regulate their behaviors (Li et al., 2019; Scaffaro et al., 2017e). Among the different approaches proposed for fabricating porous scaffolds for TE, electrospinning is one of the most investigated since permits the preparation of fibers with varying diameters, ranging from nano- to micro-scale. The process lies on polymer filaments formation, from a solution or melt, between two electrodes bearing electrical charges of opposite polarity. Once ejected from a metallic needle, the charged solution jets flows in the direction of the electric field making the solvent evaporates to become fibers (Haider et al., 2018; Zhang et al., 2017). The important advantages of electrospinning technique are the production of highly interconnected porous mats with large surface areas, superior mechanical properties and the simplicity of process combined with the possibility of large-scale productions, which make this technique very attractive for many different applications (Zhang et al., 2018).

Nowadays a plethora of advanced polymers both from synthetic (Berndt et al., 2019; Gong et al., 2019; Gu et al., 2019a; Guo et al., 2019; Ma et al., 2019; Ma et al., 2018; Yang et al., 2019) and natural sources (Shi et al., 2019b, 2019a; Xu et al., 2019) with peculiar properties has attracted widespread interest. Among these, one on the most interesting electrospinnable polymer is polylactic acid (PLA). This material has been widely studied because it is nontoxic, biocompatible and possesses interesting mechanical and physical properties (Scaffaro et al., 2017f).

Considering the wide range of potential applications of electrospun mats such as biomedical (Haider et al., 2018), environmental (Huang et al., 2017; Ray et al., 2016), electronic (Aruna et al., 2017; Guo et al., 2018), one of the major challenges in electrospinning approach is the preparation of mats with tunable properties. In this context, several process and post-process modifications of electrospun mats were proposed such as the use of multiple jets (Scaffaro et al., 2017a), fibers alignment (Scaffaro and Lopresti, 2018a; Wang et al., 2018), coaxial electrospinning (You et al., 2016), surface modifications (Rieger et al., 2013; Surucu et al., 2016), blends with other biopolymers (R. Scaffaro et al., 2018) and/or the use of micro or nanoparticles (MPs, NPs) as filler for the polymer matrix (Abdel-Mottaleb et al., 2019; Scaffaro et al., 2019). In particular, fillers are able to tune specific properties of polymers to increase their mechanical strength and/or endow them with additional features (Dong et al., 2019, 2018; L. Ma et al., 2019a, 2019b; Qian et al., 2018). In fact, composites and nanocomposites find applications in a broad range of fields such as sensors (Jiang et al., 2019), energy (An et al., 2019; Liu et al., 2017; Ma et al., 2019), anticorrosion (Zhu et al., 2019), catalysis (Chen et al., 2019; Lin et al., 2019; Pan et al., 2018). Final properties of a polymer-based composites are strongly affected by

several features that involves matrix/particles interaction including, among the others, the structure anisotropy and the particle dimension (Chan et al., 2019; Huan et al., 2018). In particular, Scaffaro and Lopresti (Scaffaro and Lopresti, 2018a), recently demonstrated that the reinforcing action of graphene nanoplatelets in PLA nanofibers is more pronounced in mats composed by aligned fibers. These showed an increase of the elastic moduli more than three times higher if compared with the randomly oriented mats. Furthermore, specific fiber arrangements could be more appropriate than conventional random mats in particular when the cells should grow along specific directions (Kuppan et al., 2016; Yang et al., 2005). Nanofibers can be aligned introducing specially designed collectors such as two parallel electrodes or by simply using a high speeds rotating collector (Scaffaro et al., 2017e).

Particle size plays important role on morphological characteristic affecting the quality of fillers as reinforcing agents (Corobea et al., 2016). Smaller particles expose more surface area per unit weight than bigger particles, thus enhancing the contact between the polymer and the filler phase that can lead to an increase of the reinforcing action (Barrera and Cornish, 2017). Bigger particles can also act as localized stress points, generating defects within the composite that can cause the fracture of the material at lower strain. Nevertheless, important drawbacks have been associated with the use of NPs, including the complexity and high cost of their production compared to macro and micro size particles (Barrera and Cornish, 2017).

Many different kinds of particles can be potentially used as filler such as TiO_2 (L. Ma et al., 2018; Tian et al., 2019), zeolites (Luo et al., 2018a), Cu_2O nanoparticles (Luo et al., 2018b), graphene (He et al., 2019; S. Li et al., 2019; Zhang et al., 2019), carbon nanotubes (P. Yang et al., 2019), carbon nanospheres (Gu et al., 2019b), ZnO (Sun et al., 2019) on the basis of the final application of the material.

In this context, scaffolds made of nanofibrous mats based on biodegradable polymers filled with hydroxyapatite (HA) have been intensely investigated in recent years (Abdal-hay et al., 2018; Miculescu et al., 2017a; Ni et al., 2019; Yang et al., 2018). HA is the main constituent (70%) of the bone tissue; when incorporated in the polymer matrix it can enhance mechanical properties, promote faster bone regeneration and induce stem cells to differentiate into osteocytes (Carfì Pavia et al., 2018; Li et al., 2018; Miculescu et al., 2017b; Milazzo et al., 2019; Vitrano et al., 2018).

Since HA properties are mainly adequate for nonload bearing applications, it is usually combined with biocompatible polymer matrix in order to obtain resorbable biocomposites (Miculescu et al., 2018; Pandele et al., 2017). Although HA was intensively investigated as biofiller for PLA, the systematic effect of particles dimension on the morpho-mechanical properties of electrospun systems has not deeply studied yet.

The novelty of this work is to compare the reinforcing effect of HA particles with different sizes i.e. micrometric (μHA) and nanometric (nHA) in PLA-based electrospun scaffold composed by aligned and randomly oriented fibers. The surface chemical composition of PLA/nHA and PLA/μHA systems was carried out with Fourier transform infrared spectroscopy in attenuated total reflectance (FTIR-ATR). The polymeric solutions were characterized by rheological measurements in order to correlate the viscosity with the morphology of the nanofibers analyzed through scanning electron microscopy (SEM). The reinforcing effect of both μHA and nHA was evaluated on aligned and randomly oriented electrospun mats through tensile tests. The crystallinity of the composites was investigated by differential scanning calorimetry (DSC). Finally, cell culture assays with pre-osteoblatic cells were conducted on the composite scaffolds in order to compare the cell proliferation and morphology on the μHA and HA PLA-based scaffolds with that of PLA scaffolds.

2. Experimental section

2.1 Materials and method

In this work, PLA (2002D) was supplied by NatureWorks while Acetone (Ac), Chloroforms (TCM) and the commercial grade nHA were purchased from Sigma Aldrich. µHA (Camceram III, HA coating powder) used was provided by Alhenia.

In order to avoid hydrolytic degradation of PLA, it was dried overnight under vacuum at 90 °C (Scaffaro and Lopresti, 2018b).

PLA/µHA and PLA/nHA electrospun composites was similar to those adopted for another electrospun system described in previous a work (Scaffaro et al., 2017d). In brief, the solvent system for PLA was TCM:Ac (2:1 vol). PLA was added to obtain a composition of 10 wt% with respect to TCM:Ac mixture and dissolved at room temperature under continuous magnetic stirring overnight. Therefore, HA particles were added to the solution and were ultrasonicated for a total of 1 h. Two different concentrations of µHA and nHA were chosen: 10 wt% and 20 wt% with respect to PLA.

A semi-industrial electrospinning equipment (NF-103, MECC CO., LTD., Japan) was used to prepare PLA nanofibers scaffolds and the biocomposites. A 5-mL syringe fitted with a 19 gauge stainless steel needle was filled with the polymeric solution. The electrospinning process was then carried out using the following constant parameters: flow rate, 1 mL/h; distance between the needle tip and the collector, 13 cm; supplied high voltage, 15 kV; temperature, 25 °C and relative humidity, 40%. The nanofibers obtained were collected on a grounded rotary drum (diameter = 10 cm) wrapped in an aluminum foil for 180 min in order to obtain membranes approximately 100 µm thick. The speed of the rotary drum was 10 rpm for the randomly oriented fibers and 200 rpm for the aligned fibers. The collected electrospun membranes were subsequently dried for at least 2 days under fume hood in order to remove any residual solvents.

The samples were coded as follow: X PLA/yHA ZZ% where X is A for the aligned systems or R for the randomly oriented mats, y is µ for micro-sized HA or n for nano-sized HA, finally ZZ% is the HA mass fraction (or weight percentage, wt%) in the composite.

2.2 Morphological analysis

The morphology of the nanofiber mats was evaluated by Scanning Electron Microscopy, (Phenom ProX, Phenom-World). The samples (4 × 4 mm) were attached on an aluminum stub using an adhesive carbon tape. Therefore, they were sputter coated with gold (Sputtering Scancoat Six, Edwards) for 90 s under argon atmosphere before imaging to avoid electrostatic discharge during the test.

2.3 Particles size and fiber diameter and orientation analysis

Particle size distribution and fiber diameter distribution of electrospun mats was determined using a dedicated image processing software. Particle size distribution was carried out by ImageJ on SEM images of HA particles while the fiber diameter distribution was conducted by using a plugin for ImageJ (DiameterJ) that permits to analyze an image obtained by SEM in order to produce a histogram of the fiber diameter distribution and of the fiber orientation (Hotaling et al., 2015).

2.4 Differential scanning calorimeter

The calorimetric properties of the composites were studied by using a Differential Scanning Calorimeter (DSC), (Setaram, model DSC131). Electrospun samples were sealed in aluminum pans with approximately the same weight (~ 10 mg). The analysis was carried out with a cycle of heating from room temperature to 200 °C at 10 °C/min under nitrogen flow.

The degree of crystallinity (χ) of PLA and PLA-based composites was calculated according to Eq. (1) (R Scaffaro et al., 2018):

$$\chi\,(\%) = \frac{\Delta H_m}{\Delta H^0{}_{PLA} \times X_{PLA}} \times 100 \quad (1)$$

where and ΔH_m is the melting enthalpy of the sample, X_{PLA} is the weight fraction of PLA. $\Delta H^0{}_m$ is the melting enthalpy of 100% crystalline PLA equal to 93.7 J/g (Scaffaro et al., 2018).

2.5 Complex viscosity of the polymeric solution

Rheological characterization tests were performed using a plate–plate rotational rheometer Mars (Thermofisher). A 25-mm parallel-plate geometry was used, and all tests were performed at 25 °C. Oscillatory frequency sweep tests were performed at a constant stress of 1 Pa with an increase of angular frequency from 1 to 100 rad/s.

2.6 Mechanical properties

Tensile mechanical measurements were carried out by using a dynamometer (Instron model 3365) equipped with a 1 kN load cell. The tests were performed on rectangular shaped specimens (10 × 90 mm) cut off from the membranes along the radial direction of the rotary drum collector, fixed to the pneumatic jaws of the dynamometer. Due to the high elongation of the samples, the measurements were performed by using a double crosshead speed: 1 mm·min^{-1} for 2 min and then

50 mm·min^{-1} until fracture. The thickness of each sample was measured before test whereas the gauge length was 20 mm for all the samples. The representative nominal stress-strain curves were reported for each material. The elastic modulus (E) was calculated from the slope of the initial part of the engineering stress-strain curves. Seven samples were tested for each material and the average values of the mechanical parameters were reported with their standard deviations.

2.7 *In vitro* cell cultures

Pre-osteoblastic MC3T3-E1 cells (Sigma Aldrich) were cultured in Dulbecco's modified Eagle's medium (DMEM, Sigma Aldrich) supplemented with 10% of fetal bovine serum, 1% of glutamine and 1% of streptomycin/penicillin in 75 cm^2 cell culture flasks incubating at 37 °C with 5% CO_2. Pure PLA and A PLA/nHA 20% scaffolds were reduced to square-shaped samples (area about 1 cm^2). The samples were sterilized under U.V. light for 2 hours and pre-conditioned O.N. with complete culture medium. Cells were detached from the culture flasks with the standard protocol using the tripsyn/EDTA solution and counted through a Burker chamber. Thereafter, 40 µl of cellular suspension were kindly inoculated onto each scaffold at the concentration of 5x10^4 cells/cm^2. After an incubation at 37°C and 5% CO_2 for 90 minutes to promote cell adhesion, each scaffold was transferred into a well of a 24 well plate and fresh medium was added. The culture was conducted up to 10 days.

2.8 Cells viability assay

The proliferation rate was evaluated used an AlamarBlue Cell Viability Reagent (Invitrogen). After scaffolds transfer into other wells (to avoid the quantification of cells adhered to well), each sample was incubated at 37°C and 5% CO_2 for 3 hours with 500 µl of a Alamar Blue reagent (10X) diluted (1:10) in DMEM; the samples were incubated with this solution for 2hrs at 37°C. The resulting fluorescence was read on a plate reader; excitation wavelength was 530/25 (peak excitation is 570nm); emission wavelength was 590/35 (peak of emission is 585nm). The amount of fluorescence produced is proportional to the number of living cells. The assays were carried out at 1 (T1), 6 (T6), 8 (T8) and 10 (T10) days of culture in triplicate for each time. Not seeded scaffolds were used as negative controls in each measurement.

2.9 Analysis of the cell morphology on the scaffolds surface

Electrospun scaffold, after a culture in the incubator, were put into a 24-well polystyrene plate and washed 4 times with complete 1X PBS. For the fluorescence analysis, the samples were fixed with

formaldehyde solution 3.6% for 15 min at room temperature and then they were thoroughly washed twice in the 1X PBS. The fixed cells were stained with Alexa Fluor Phalloidin 488 (Thermo Fisher Scientific and nuclei with 4′,6-diamidino-2-phenylindole (DAPI; Merck KGaA) for 30s at room temperature. Images were taken under a fluorescence microscope (Leica DM 2500, Leica MicroSystems) equipped with a charge-coupled device camera. All tests were performed in triplicate. A SEM analysis was performed to observe MC3T3-E1 cells onto electrospun scaffolds. Samples were washed with fresh DPBS pH 7.4 and fixed with glutaraldehyde 4% (v/v) at 4°C for 2 h, then were rinsed with water and dehydrated with ethanol series (25%, 50%, 75% v/v and pure ethanol). Finally samples were dried under vacuum prior to be gold sputtered and analyzed by SEM at the same conditions described above

2.10 Statistical analysis

Statistical analyses of the data were performed through ANOVA by using the GraphPad Prism version 6 software (GraphPad Software Inc., La Jolla, CA, USA). Significant differences among mean values, where applicable, were determined by the means of ANOVA and by Tukey′s post hoc test for multiple comparisons. In all cases, a value of $p<0.05$ was considered statistically significant.

3. Results

3.1 Structure of the electrospun nanofibers and solution viscosity

In Fig. 1A,B SEM images of micrometric and nanometric HA used in this work after sonication are reported. The morphology of µHA is characterized by irregular aggregates having different dimensions. In particular, the particles size distribution (Fig. 1C) shows both aggregates with diameter ranging from 10 µm up to 60 µm (the size distribution in Fig. 1C stops at 20 µm because of the low number of big particles and for the sake of comparison with Fig 1D) and particles with diameter lower than 1 µm. As evident in the inset of Fig. 2A, µHA particles were found to be remarkably wrinkled and crumpled, surrounded by the smaller, nanometric power. Differently, the morphology of nHa appeared smoother and more regular if compared with µHA. The shape is almost spherical (inset in Fig. 2B') and the size of the aggregates never exceeded 5 µm with a peak of distribution at 190 nm (Fig. 2D), in line with that declared by the supplier.

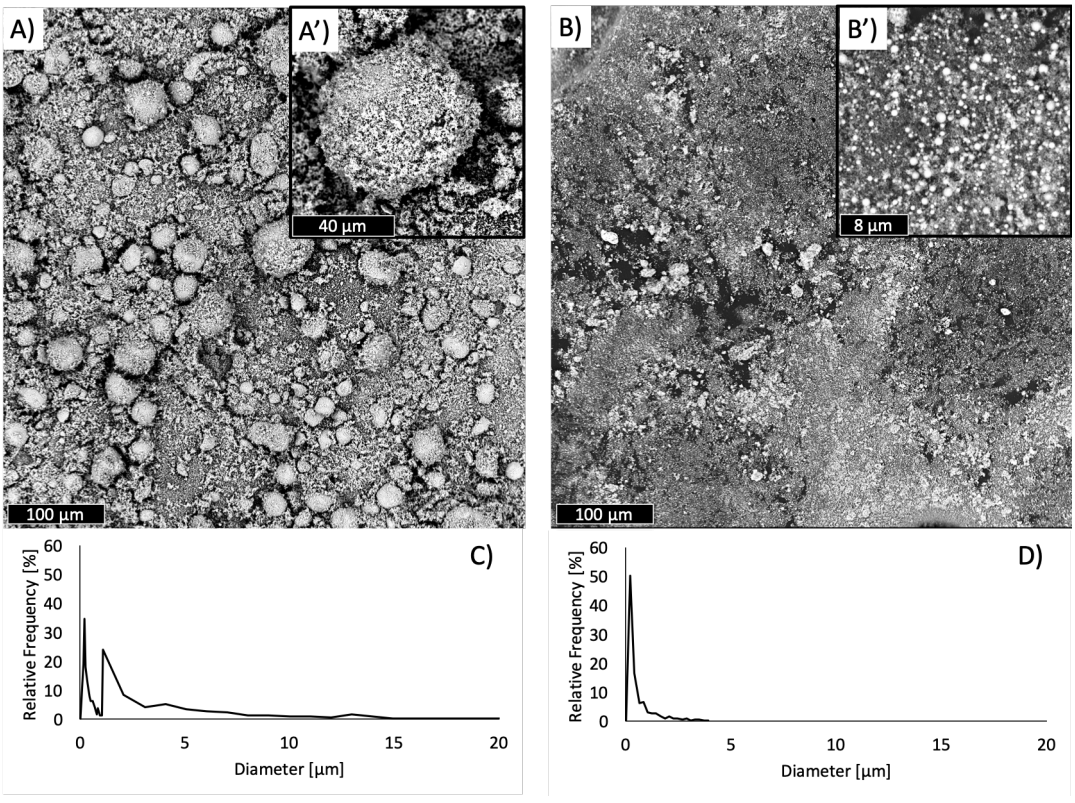

Figure 1 - SEM micrographs of A) µHA and B) nHA. Particle size distribution of C) µHA and D) nHA

In Fig. 2 ATR-FTIR measurements carried out on electrospun PLA, µHA and nHA powders are shown, as well as on all PLA/HA composites mats.

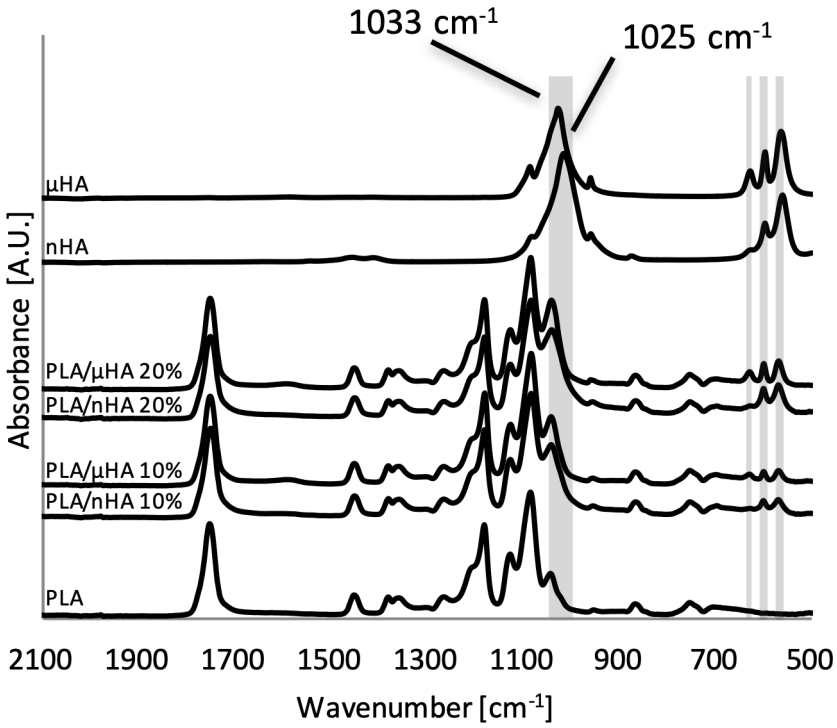

Figure 2 –ATR-FTIR carried out on µHA and nHA particles, electrospun PLA and PLA/HA composites.

The spectra of PLA showed the typical peaks of the polymer such as the carbonyl stretch at 1747 cm^{-1}, the CO stretch at 1180 cm^{-1}, 1129 cm^{-1} and 1083 cm^{-1} and the OH bend at 1044 cm^{-1} (Scaffaro et al., 2017b). The FTIR-ATR of the two kind of HA are slightly different. Specifically, both the systems showed the PO_4 bend (ν_β) at 1092 cm^{-1}, PO_4 stretch (ν_1) at 962 cm^{-1}, PO_4 bend (ν_4) at 601 cm^{-1} and 565 cm^{-1} (Panda et al., 2003). PO_4 bend (ν_4) of µHA and nHA are slightly shifted at 1033 cm^{-1} and 1025 cm^{-1} respectively. Moreover, the structural OH (at 635 cm^{-1}) is much more visible in µHa while it is a shoulder for nHA powder. The latter presented a small peak at 873 cm^{-1} indicative of the carbonate ion substitution (Stoch et al., 2000) not present in µHA particles.

In the case of PLA/HA composites, part of the HA bands were overlapped by the more intense PLA peaks. PO_4 bend at 601 cm^{-1} and 565 cm^{-1} and the structural OH at 635 cm^{-1} of HA can be easily depicted also in PLA/HA composites, since they were not overlapped with PLA peaks and they showed no wavelength shifts with respect to the raw powder. Furthermore, it can be noticed that the peak intensity related with HA included in PLA increased upon increasing the filler concentration in the composites. It is also possible to observe that the OH band (1044 cm^{-1}) intensity increased upon increasing the HA concentration within the composite membranes because of the influence of PO_4 bend (ν_4) of HA occurring in the same region of the spectrum. SEM micrographs of the random and aligned electrospun PLA and its composite are presented in Fig. 3 associated with their corresponding diameter distribution and fiber orientation. The micrograph of the random electrospun PLA shows the typical morphology of an electrospun material with fibers in the nanoscale and randomly oriented.

In Fig. 3 the A PLA mats showed a moderate aligned structure, composed by smooth and homogenous fibers with diameter comparable with that of random system. All PLA/HA composites produced in this work showed a mean fiber diameter higher than electrospun PLA. Moreover, a noticeable difference in mean fiber diameter between random and aligned fibers can be observed in composites mats. Specifically, the fiber diameter of random mats is approximately 10-20% higher than aligned one. Furthermore, the diameter size distribution of aligned fiber is narrower than random systems. The dispersion degree of μHA and nHA is noteworthy but HA agglomerates ranging from 5 up to 20 μm can be observed in PLA/μHA composites inducing the formation of irregular bump in the fibers. In PLA/nHA composites the HA nanoparticles are clearly visible on the surface of the fibers and their number increase upon increasing the nHA concentration.

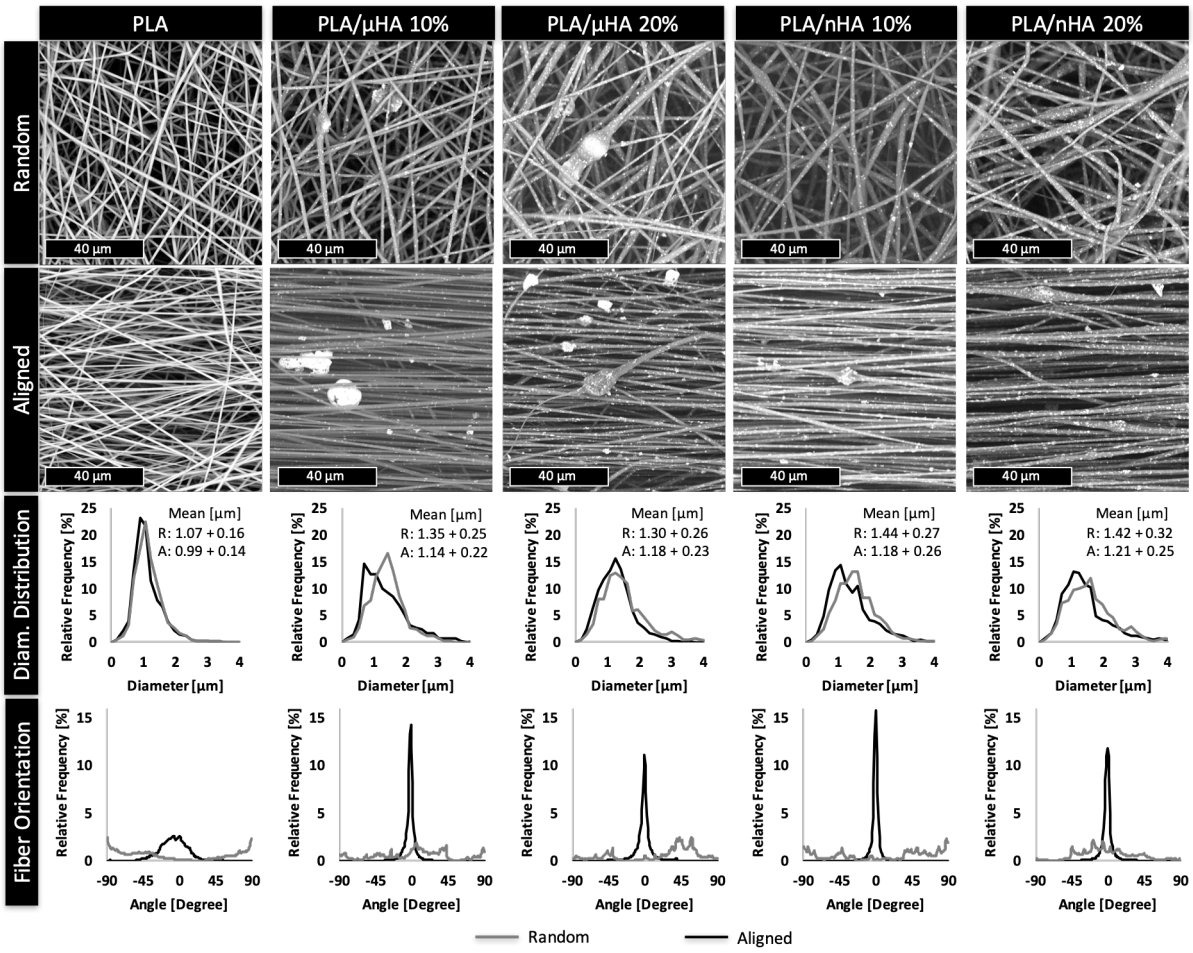

Figure 3 - SEM micrographs of random and aligned electrospun mats at different μHA and nHA concentration and their corresponding fiber diameter and fiber orientation distribution.

It is possible to notice some small agglomerates not higher than 4 μm also in PLA/nHA composites. HA nanoparticles are also visible in PLA/μHA composites but in lower number if compared with PLA/nHA at the same filler concentration. When compared to A PLA electrospun mats, the fiber orientation distribution of aligned composites mats, was more homogenous and well defined, and

seems not to depend on the filler dimension. More specifically, it is possible to observe that the fiber orientation distribution of composites containing 10% of filler is more homogenous than that of composites filled with 20% for both PLA/µHA and PLA/nHA composites.

It is well known that, generally, an increase of the solution viscosity leads to electrospun fibers with larger average diameters (Scaffaro and Lopresti, 2018a; Zhou et al., 2013). In order to evaluate the correlation between the viscosity and the fiber diameter of electrospun mats, the complex viscosity of PLA solution, as well as PLA/µHA and PLA/nHA suspensions were measured as a function of frequency (Fig. 4). As expected, PLA/HA suspensions showed higher viscosity if compared with PLA solution at the higher frequency investigated and it slightly increased upon increasing HA amount and upon decreasing the particles dimension.

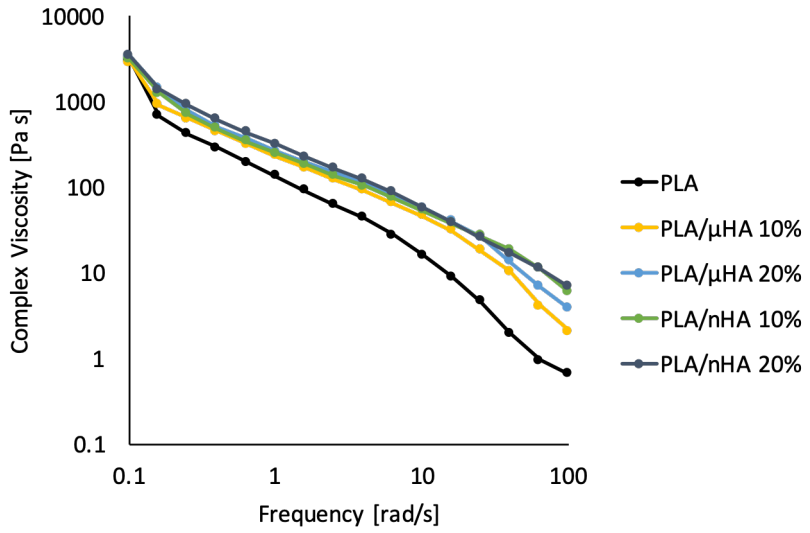

Figure 4 - Complex viscosity of the PLA solution and PLA/µHA and PLA/nHA suspensions.

3.2 Mechanical and thermal properties

Fig. 5 A,B displays representative engineering stress-strain curves of randomly oriented and aligned electrospun mats as a function of µHA and nHA concentration, respectively. At low strain region of random mats (Fig. 5A) it can be observed some vibrating points that can be explained with the low force opposed by the electrospun mats due to their high porosity. The cusp points at 10% strain are due to the change of the crosshead speed. From Fig. 5A,B it is possible to observe that PLA electrospun mats showed the typical mechanical behavior of a ductile material exhibiting a relative low elastic modulus (E) and a relative high elongation at break (ε).

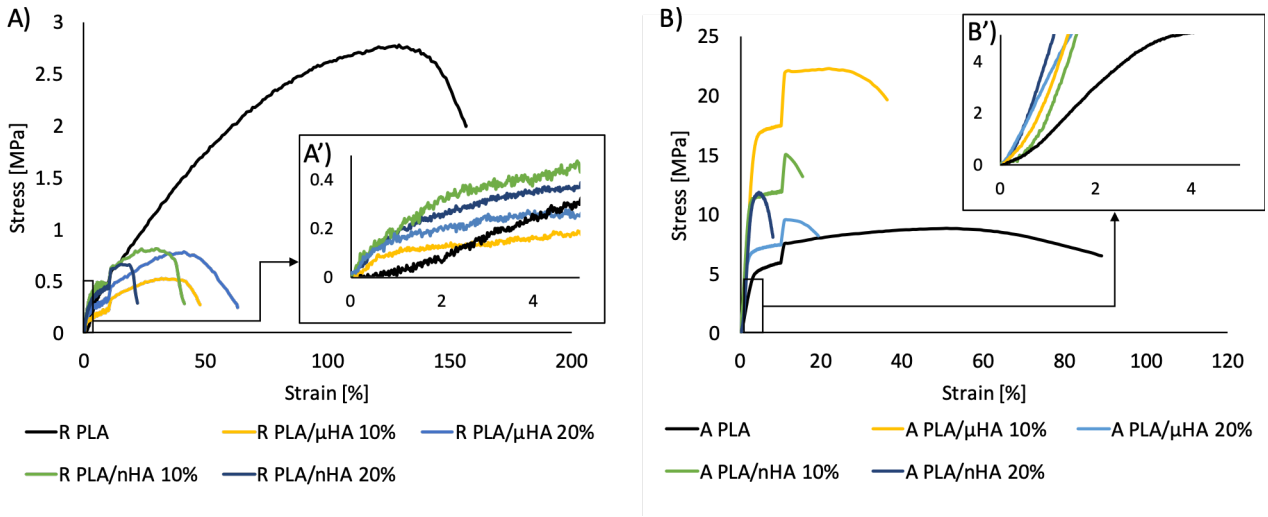

Figure 5 - Representative stress-strain curves of (A,A') randomly oriented and (B,B') aligned electrospun mats.

The presence of filler made all the composites more brittle than PLA exhibiting a strong reduction of elongation. The premature failure of random mats induced a reduction of the tensile strength while for aligned systems it is possible to observe an increase of this parameter. In Fig. 5A it is possible to observe a monotonic increase of the R PLA stress strain curves, while in Fig. 5B it is possible to observe a relative long plateau of the stress strain curve of A PLA.

In Fig. 6A-F the elastic modulus (E), the tensile strength (TS) and the elongation (ε) obtained from the stress-strain curves for both random and aligned mats are reported.

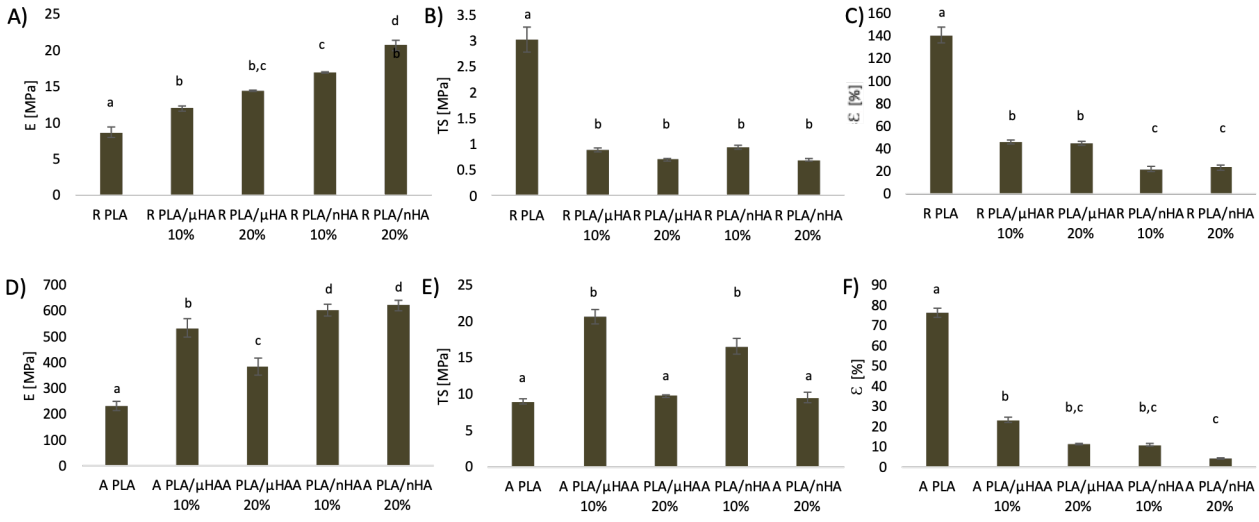

Figure 6 – A) Elastic modulus, B) tensile strength and C) elongation of the randomly oriented electrospun mats. D) Elastic modulus, E) tensile strength and F) elongation of aligned electrospun mats. Values are given as means ± SD. Different letters in the same graph indicate significant differences ($p<0.05$) when analyzed by Tukey's multiple comparisons tests.

The data put into evidence that the elastic modulus of the randomly oriented fibrous structures filled with µHA or nHa (Fig. 6A), significantly increased if compared with electrospun PLA. At the same

time both tensile strength and elongation of randomly oriented mats significantly decreased if compared with electrospun R PLA (Fig. 6B,C). Similarly, the elastic modulus of the aligned composites containing µHA or nHA (Fig. 6D) significantly increased if compared with PLA mats. The tensile strength was significantly higher than that of electrospun PLA for composites containing 10% of both µHA and nHA while it was statistically comparable with that of A PLA mats when the concentration of fillers was 20% (Fig. 6E). The elongation of aligned composites mats significantly decreased if compared with electrospun PLA (Fig. 6F). The dimensionless values of the elastic modulus, tensile strength and elongation at break are reported in Figs. 7A-C for all the samples as a function of the filler concentration. The dimensionless values were obtained by dividing the values of each mechanical property of both randomly oriented or aligned mats at any given filler concentration by the respective value of the randomly oriented or aligned PLA samples (La Mantia et al., 2018).

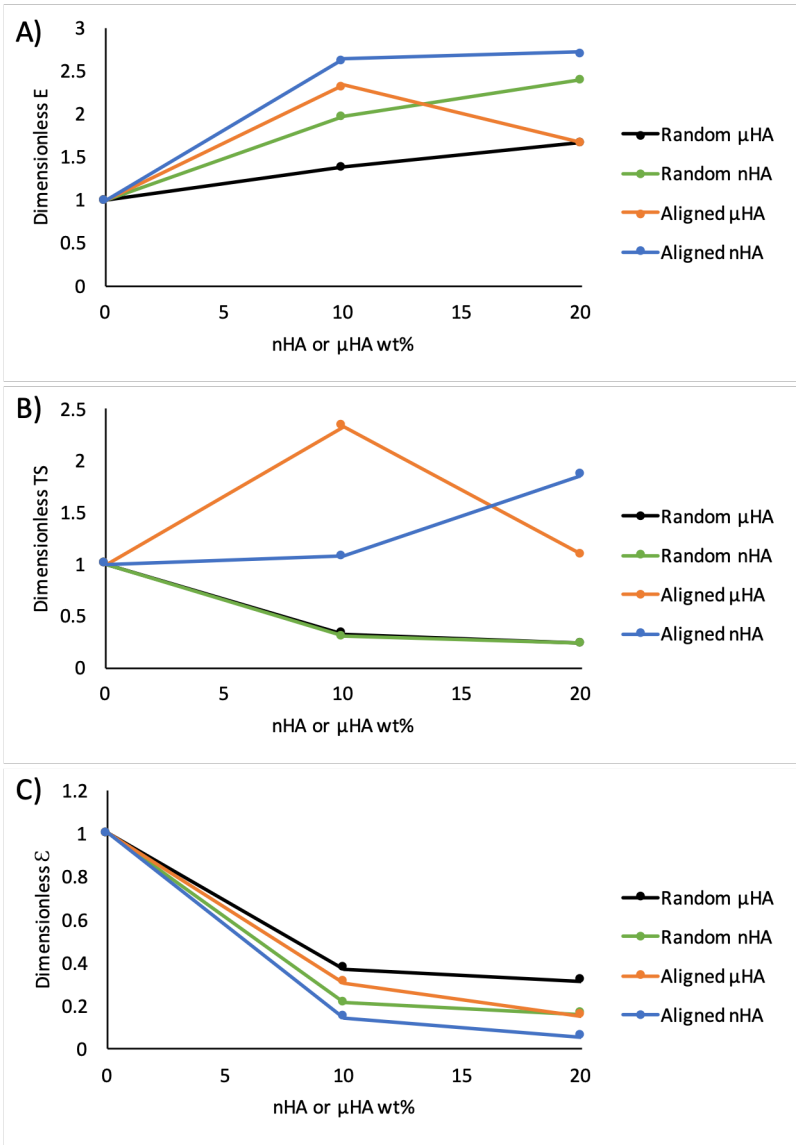

Figure 7 - Dimensionless A) elastic modulus; B) tensile strength and C) elongation of electrospun PLA and nanocomposite as a function of fillers concentration

As observed in Figs. 7A, elastic modulus increased almost linearly with the filler concentration except the A PLA/μHA mats. More in detail, if compared with R PLA, the elastic modulus increase was found to be approximately 40% for the system filled with μHA at 10%, 70% for the systems R PLA/μHA 20%, 100% for R PLA/nHA 10% and up to 140% for the R PLA/nHA 20% composite (Fig. 7A). On the other hand, for aligned system, the increase of elastic modulus (Fig. 7A) due to both μHA and nHA is also higher than that observed for the random composites. In fact, A PLA/μHA 10% and 20% exhibited an increase of the elastic modulus of ~130% and ~70% respectively, while the E increase observed for A PLA/nHA 10% and 20% is around 160% and 170%, respectively making A PLA/nHA 20% the best system in terms of elastic modulus improvement.

The tensile strength (Fig. 7B) of the random PLA/HA composites is 68-70% lower than that of R PLA regardless the dimension and the amount of filler, while TS of aligned mats containing 10% of μHA and nHA is ~130% and ~84% respectively higher than that of A PLA. Aligned composites containing 20% of μHA and nHA showed a TS comparable with that of A PLA mats. The elongation (Fig. 7C) of PLA/μHA and PLA/nHA systems resulted ~70% and ~85% respectively lower than that of PLA, independently from the amount of filler and the fiber orientation.

According to these results, is evident that the reinforcing effect in PLA filled with 20% of nHA is around 150% higher than that of 20% of μHA. About the reinforcing effect of HA in aligned and randomly oriented mats it is easy to observe that the increment of the elastic modulus of A PLA/μHA 10% and A PLA/nHA 10% are ~240% and ~70% higher, respectively, if compared with that of the corresponding randomly oriented mats. For the same systems filled with 20% of particles the increment is negligible for μHA and was found to be ~20% for nHA.

DSC analysis were carried out in order to investigate the effect of μHA and nHA on the crystallization behavior of electrospun PLA. In Fig. 8A the crystallinity of the mats evaluated according to Eqn. 1 is reported, while in Fig. 8B the melting temperatures (T_m) (evaluated as the temperatures corresponding to the maximum of the melting peak) are reported.

Results in Fig. 8A highlighted that the crystallinity of R PLA and A PLA mats are 12% and 13% respectively. A slightly χ increase was observed upon increasing both μHA and nHA content and χ seemed to be also dependent on the fiber's orientation. Specifically, if compared with R PLA, it is possible to observe an increase of χ of ~70% and ~100% for R PLA/μHA 10% and 20%, respectively, while for the corresponding aligned systems, the χ increase was only 24 % and 46%. Similarly, R PLA/nHA 10% and 20% showed an increase of χ respectively of 69% and 90% if compared with R PLA while the increase for A PLA/nHA 10% and 20% in comparison with A PLA is ~42% and ~57%, respectively.

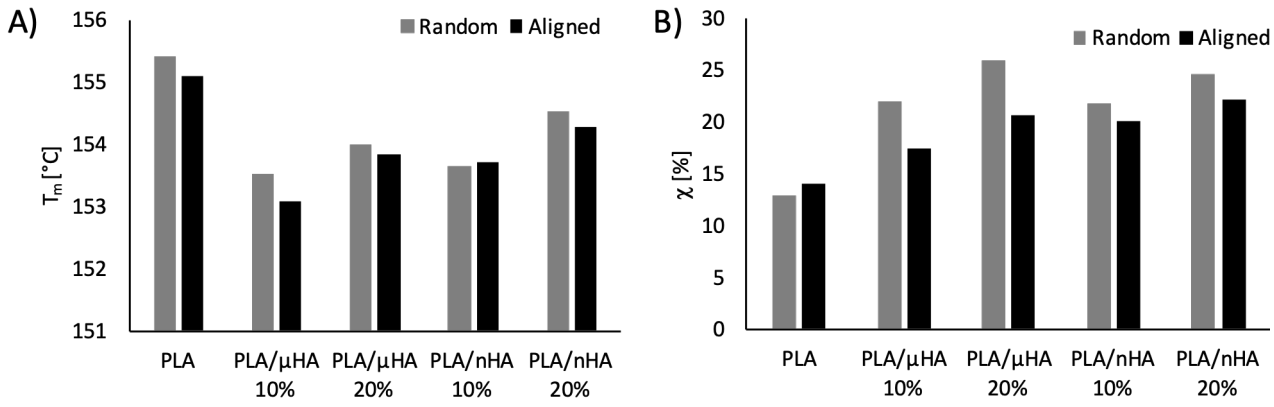

Figure 8 – A) Melting temperature (T_m) and B) crystallinity (χ) of PLA-based electrospun mats.

In Fig. 8B it is easy to note that the addition of µHA and nHA particles slightly reduced the T_m of PLA. Regardless the fiber orientation, electrospun PLA displayed a T_m around 155°C while it reached ~153°C and ~153.5 °C for PLA/µHA 10% and 20% respectively and ~153.5°C and ~154.5 °C for PLA/nHA 10% and 20% respectively.

3.3 Cell culture

The cytocompatibility of composite scaffold (A PLA/nHA 20%) was assessed by in vitro cell tests in terms of attachment and proliferation of MC3T3-E1 pre-osteobastic cells. For this study A PLA/nHA 20% samples were chosen since it was found to be the best system in terms of elastic modulus improvement.

Alamar assay was carried out to study the viability of cells seeded on A PLA (used as control) and composite scaffolds. The absorbance values have been normalized to the value obtained 24h after the seeding and reported in Fig. 9A.

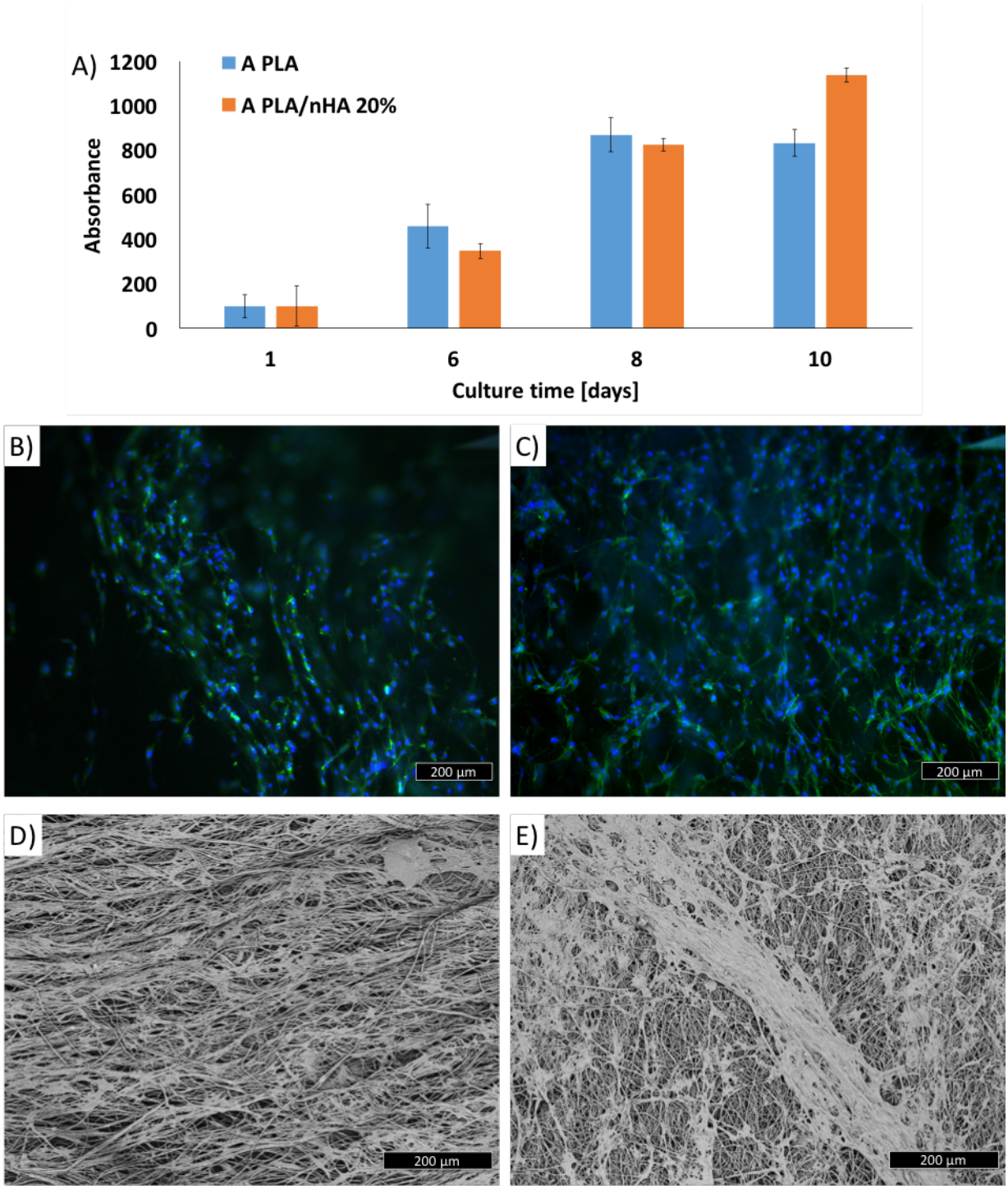

Figure 9 – A) MC3T3-E1 viability assays on scaffolds of PLA (blue) and PLA/HA (orange); Fluorescence microscopy images of MC3T3-E1 cells grown on PLA/HA (B) and pure PLA (C) scaffolds; SEM micrographs of MC3T3-E1 cells grown on PLA/HA (D) and pure PLA (D) scaffolds.

From the whole culture time taken in consideration, viable cell number increased on both substrates. The trends overlap for both scaffolds, without statistically significant differences, demonstrating a comparable biocompatibility.

Figure 9B–C shows representative images of the MC3T3 cells attached on the substrates after 10 days of culture. From these images, where the nuclei are stained in blue and the cytoskeleton appears in

green, it is possible to observe that the cells adhere to the matrix and appears well spread in both cases. This morphology suggests good cytocompatibility as previously confirmed by Alamar assay. Moreover, it is easy to notice that the cells grown on composite scaffold appear more aligned with respect those grown on PLA mats. The result was confirmed by SEM images (Fig. 9D,E). As a matter of fact, pure PLA scaffold are characterized by the presence of groups of cells randomly disposed, whereas in composite scaffold it is possible to observe a homogenous cellular distribution along the fibers. This cells behavior could be attributed to the presence of nHA that, according to a previous work (Domingos et al., 2017), promotes cell-cell contact and subsequent tissue organization.

4. Discussion

HA has been commonly used as PLA filler for bone regeneration purposes due to its excellent physicochemical properties such as osteoconductivity. In this context, HA particles dimensions can affect the cell response as well as its reinforcing effect on a polymeric matrix (Milazzo et al., 2019). In order to assess the reinforcing effect of HA particles with different sizes on randomly oriented and aligned PLA nanofibrous mats, two different HA particles were chosen in this work. As visible from Fig. 2A-D, the μHA showed a bimodal size distribution with two peaks at 0.22 μm and 1.12 μm, while the nHA particles exhibited a narrower size distribution with a unique peak at 0.21 μm. The FTIR-ATR measurements conducted on PLA/μHA and PLA/nHA systems, clearly showed the characteristic peaks of both the polymer matrix and the respective particles, thus confirming the successful inclusion of the filler in the PLA nanofibers. The absence of wavelength shifts in PLA/HA composites with respect to the raw PLA and HA provides a first indication that their structure is not strongly modified during the electrospinning process.

Also, the structural OH peak (at 635 cm^{-1}), more visible in μHa particles, is still higher in PLA/μHA composites while the small peak at 873 cm^{-1} indicative of the carbonate ion substitution (Stoch et al., 2000) in nHA is not visible in composites since it is covered by the -C-C- stretch of the PLA crystalline phase at 869 cm^{-1} (Scaffaro et al., 2016). Furthermore, from the same figure, it is evident that the systems containing 20% of particles showed a higher intensity of the representative band of μHA and nHA if compared with composites loaded with 10% of HA, thus corroborating the effective inclusion of higher concentration of particles.

The morphology of PLA-based electrospun scaffolds was found to be affected by both the filler dimension and their weight concentration that are both related with the solution viscosity. For instance, the fiber diameter of randomly oriented and aligned PLA/μHa and PLA/nHA composites is higher than that of PLA mats. In order to likely explain these results, it may be considered that

electrospinning process relies on the phenomenon of the uniaxial stretching of a charged jet. The stretching of the charged jet is significantly affected by changes in polymeric solution viscosity. In fact, the higher the shear viscosity, the higher the resistance to flow; therefore, the diameter of the fibers will increase upon increasing the solution viscosity, as confirmed by other theoretical and experimental works (Haider et al., 2018; Lu et al., 2006; Reneker and Yarin, 2008; Scaffaro and Lopresti, 2018a). Usually, the presence of solid particles increases the complex viscosity of polymeric solutions except for nanoparticles acting as plasticizers (Zhang et al., 2016) or presenting pro-degradative effects (Du et al., 2016). In this work, as expected and coherently with the fiber diameter distribution of the mats, both μHA and nHA induced an increment of the complex viscosity of the polymer solution and a consequent increase of the fiber diameter. At the same time, the aligned fibers are always smaller than the corresponding systems randomly oriented, as already observed previously (Scaffaro and Lopresti, 2018a). Furthermore, the higher alignment degree observed in composites mats, can be likely ascribed at the higher viscosity of the solution. In fact, by increasing the solution viscosity, the polymeric bending instability of the jet ejected from the Taylor cone is reduced and the jet path toward the collector is straighter thus providing the possibility to obtain highly aligned nanofibers on the collector (Dabirian et al., 2011). On the other hand, both A PLA/μHA and A PLA/nHA composites showed a slightly more heterogenous orientation distribution if filled with 20% of particles and compared with composites at 10% of concentration. This result can be likely ascribed to the high number of particles that can compromise the stability of the jet during its travel to the collector.

About the filler dispersion, it can be noticed that the particles size of μHA after processing seemed to be slightly lower than pristine ones. In particular the biggest particles incorporated in the fibers never exceeded 25μm while μHA particles were characterized by particles up to 60 μm. This result can be related to two main phenomena: i) the sedimentation of biggest aggregates at the bottom of the syringe and ii) the more significant shear stresses to which the solution and the particles are subjected during their paths to the collector that can likely break up the biggest particles into smaller parts.

The stress strain curves of PLA and PLA/HA composites were found to be strongly affected by the fiber orientation. The monotonic increase of the stress-strain curve of R PLA until fracture (Fig. 5A) can be related to the fibers orientation during the axial deformation that gradually increases the strength of the mat. This phenomenon can not happen in A PLA mats that, in fact, showed a plateau in the plastic deformation region of the stress strain curves (Fig. 5B). Furthermore, also A PLA/μHA 10% displayed a small plateau in that region while for the other aligned PLA/HA composites it is not possible to observe any plateau because the fracture occurs near the elastic region.

As already observed in other works (Milazzo et al., 2019), μHA and nHA are able to increase the elastic modulus of the nanofibrous mats with differences related to the filler dimension and the fiber orientation. Specifically, the nHA reinforcing effect is more than double that of μHA in randomly oriented mats, for both the concentration here investigated. This result can be ascribed to the higher surface area exposed by nHA that reasonably eased the interfacial contact between the filler and the polymer (Barrera and Cornish, 2017; R Scaffaro et al., 2018). A similar result was observed in aligned systems. If compared to A PLA, A PLA/nHA 10% elastic modulus increment is approximatively 20% higher than that observed for A PLA/μHA 10%. The improvement of the elastic properties induced by nHA are even more evident for aligned composites filled with 20% of particles, thus corroborating the hypothesis that nHA reinforcing effect is superior that that of μHA because, at higher concentrations, the microparticles aggregation act as localized stress points, generating defects within the composite that can reduce the elastic modulus of the mats (Scaffaro et al., 2017c). The better dispersion observed for nHA is able to reduce the number of defects thus maintaining a reinforcing effect also at higher concentration.

Regarding the effect of the fiber orientation on the reinforcing effect of μHA and nHA, it can be noticed that, if compared with the corresponding PLA mats, all aligned composites exhibited an increase of the elastic modulus higher than that observed for random systems. This is particularly evident for systems filled with 10% of both μHA and nHA particles, whereas it is less remarkable for both A PLA/μHA 20% and A PLA/nHA 20%. These marked improvements of the elastic properties in aligned systems can be ascribed to both i) the higher alignment degree of composites with respect to A PLA due to the presence of filler and ii) a more efficient reinforcing action of μHA and nHA on the aligned nanofibrous mats as already observed in a similar system (Scaffaro et al., 2017c).

Electrospun PLA usually exhibits crystallinity much lower than that of PLA in pellets because of the high speed of solidification during the process (Ribeiro Neto et al., 2012). Considering the increment of the crystallinity and the reduction of T_m due to the presence of both μHA and nHA, it can be assumed that both the fillers acted as a nucleating agent for PLA, as already observed in another work (Ribeiro Neto et al., 2012). The increment of crystallinity can be considered another element able to enhance the elastic modulus of the composite mats if compared with electrospun PLA, although it cannot explain the improvements of the elastic properties in aligned systems since the crystallinity of random mats is slightly higher than that of aligned systems.

The tensile strength of all the randomly oriented composites here investigated are significantly lower than that of R PLA (Fig. 6B). This result can be explained by observing the stress-strain curves in Fig. 5 and the elongation data in Fig. 6C, showing that R PLA/μHA and R PLA/nHA composites are more rigid than R PLA mats but less deformable, i.e. the failure occurred prematurely for the

composites thus inducing smaller TS values. The low deformability of the mats is even more pronounced in the aligned systems but in this case, it can be observed that TS is equal or higher than that of A PLA (Fig 6D). More in detail, for aligned composites containing 10% of particles, TS was higher than that of A PLA while it was almost equal to the pristine system in presence of 20% of particles. For these systems, it can be assumed that the superior increase of the elastic properties is able to overcome the premature fracture of the mats thus resulting in tensile strength equal or higher than that of A PLA.

Preliminary biological in vitro test confirmed the biocompatibility of the proposed devices. Moreover, results put into evidence that the presence of HA seems to induce a more homogeneous colonization of the scaffold by pre-osteoblastic cells that appear also more aligned with respect those observed in pristine PLA scaffolds.

5. Conclusion

In this work the reinforcing effect of μHA and nHA particles on PLA-based electrospun scaffold in randomly and aligned fibers orientation was evaluated. FTIR-ATR demonstrated the successful inclusion of HA particles in PLA fibers that leads to a slight increase of the composites mean fiber diameter and to a more homogenous orientation distribution of aligned composites. These morphological results can be ascribed to the solution viscosity that increased upon increasing the particles amount and upon reducing the HA size. Both μHa and nHA increased the elastic modulus of the electrospun mats although nHA reinforcing effect is higher than that of μHA. PLA/μHA were characterized by a much brittle behavior if compared with electrospun PLA or with PLA/nHA, probably because of the bigger dimension of μHA fillers that acted as a local defect. The increment of the elastic modulus due to HA particles in mats made by aligned fiber is higher than that observed in randomly oriented fibers, thus demonstrating that the reinforcing action of HA is more pronounced in aligned fibers. DSC analysis revealed that both μHA and nHA acted as a nucleating agent for PLA since they slightly increased the crystallinity and reduced T_m of PLA. Preliminary biological in vitro test confirmed the biocompatibility of the proposed devices and that nHA induced a more homogeneous colonization of the scaffold by pre-osteoblastic cells that appeared more aligned with respect those observed in A PLA scaffolds. Based on the results, we can convince that the A PLA/nHA 20% can be one of great potential biomaterials for bone tissue regeneration.

References

Abdal-hay, A., Abbasi, N., Gwiazda, M., Hamlet, S., Ivanovski, S., 2018. Novel polycaprolactone/hydroxyapatite nanocomposite fibrous scaffolds by direct melt-electrospinning writing. Eur. Polym. J. 105, 257–264. https://doi.org/10.1016/j.eurpolymj.2018.05.034

Abdel-Mottaleb, M.M., Khalil, A., Karim, S.A., Osman, T.A., A.Khattab, 2019. High performance of PAN/GO-ZnO composite nanofibers for photocatalytic degradation under visible irradiation. J. Mech. Behav. Biomed. Mater. 96, 118–124. https://doi.org/10.1016/j.jmbbm.2019.04.040

An, Y., Wu, L., Chen, H., Li, Z., Dou, H., Murugadoss, V., Fan, J., Mai, X., Zhang, X., Guo, Z., others, 2019. Metal-free Energy Storage Systems: Combining Batteries with Capacitors based on Methylene Blue Functionalized Graphene Cathode. J. Mater. Chem. A.

Aruna, S.T., Balaji, L.S., Kumar, S.S., Prakash, B.S., 2017. Electrospinning in solid oxide fuel cells--A review. Renew. Sustain. Energy Rev. 67, 673–682.

Barrera, C.S., Cornish, K., 2017. Processing and mechanical properties of natural rubber/waste-derived nano filler composites compared to macro and micro filler composites. Ind. Crops Prod. 107, 217–231. https://doi.org/10.1016/j.indcrop.2017.05.045

Berndt, A.J., Hwang, J., Islam, M.D., Sihn, A., Urbas, A.M., Ku, Z., Lee, S.J., Czaplewski, D.A., Dong, M., Shao, Q., others, 2019. Poly (sulfur-random-(1, 3-diisopropenylbenzene)) based mid-wavelength infrared polarizer: Optical property experimental and theoretical analysis. Polymer (Guildf). 176, 118–126.

Carfì Pavia, F., Conoscenti, G., Greco, S., La Carrubba, V., Ghersi, G., Brucato, V., 2018. Preparation, characterization and in vitro test of composites poly-lactic acid/hydroxyapatite scaffolds for bone tissue engineering. Int. J. Biol. Macromol. 119, 945–953. https://doi.org/10.1016/j.ijbiomac.2018.08.007

Chan, K., Kit-Hon Tsoi, J., Wu, O.-K., Jon-Yu Yon, M., Wing-Kit Wong, R., 2019. Mechanical and biological evaluations of novel electrospun PLLA composite scaffolds doped with oxide ceramics. J. Mech. Behav. Biomed. Mater. 97, 229–237. https://doi.org/10.1016/j.jmbbm.2019.05.024

Chen, Q., Yin, Q., Dong, A., Gao, Y., Qian, Y., Wang, D., Dong, M., Shao, Q., Liu, H., Han, B.-H., others, 2019. Metal complex hybrid composites based on fullerene-bearing porous polycarbazole for H2, CO2 and CH4 uptake and heterogeneous hydrogenation catalysis. Polymer (Guildf). 169, 255–262.

Corobea, M.C., Muhulet, O., Miculescu, F., Antoniac, I.V., Vuluga, Z., Florea, D., Vuluga, D.M., Butnaru, M., Ivanov, D., Voicu, S.I., others, 2016. Novel nanocomposite membranes from cellulose acetate and clay-silica nanowires. Polym. Adv. Technol. 27, 1586–1595.

Dabirian, F., Hosseini Ravandi, S.A., Pishevar, A.R., Abuzade, R.A., 2011. A comparative study of jet formation and nanofiber alignment in electrospinning and electrocentrifugal spinning systems. J. Electrostat. 69, 540–546. https://doi.org/10.1016/j.elstat.2011.07.006

Domingos, M., Gloria, A., Coelho, J., Bartolo, P., Ciurana, J., 2017. Three-dimensional printed bone scaffolds: The role of nano/micro-hydroxyapatite particles on the adhesion and differentiation of human mesenchymal stem cells. Proc. Inst. Mech. Eng. Part H J. Eng. Med. 231, 555–564. https://doi.org/10.1177/0954411916680236

Dong, M., Li, Q., Liu, H., Liu, C., Wujcik, E.K., Shao, Q., Ding, T., Mai, X., Shen, C., Guo, Z., 2018. Thermoplastic polyurethane-carbon black nanocomposite coating: fabrication and solid particle erosion resistance. Polymer (Guildf). 158, 381–390.

Dong, M., Wang, C., Liu, H., Liu, C., Shen, C., Zhang, J., Jia, C., Ding, T., Guo, Z., 2019. Enhanced Solid Particle Erosion Properties of Thermoplastic Polyurethane-Carbon Nanotube Nanocomposites. Macromol. Mater. Eng. 304, 1900010.

Du, X., Xu, X., Liu, X., Yang, J., Wang, Y., Gao, X., 2016. Graphene oxide induced crystallization and hydrolytic degradation of poly (butylene succinate). Polym. Degrad. Stab. 123, 94–104.

Gong, X., Liu, Y., Wang, Y., Xie, Z., Dong, Q., Dong, M., Liu, H., Shao, Q., Lu, N., Murugadoss, V., others, 2019. Amino graphene oxide/dopamine modified aramid fibers: preparation, epoxy nanocomposites and property analysis. Polymer (Guildf). 168, 131–137.

Gu, H., Xu, X., Cai, J., Wei, S., Wei, H., Liu, H., Young, D.P., Shao, Q., Wu, S., Ding, T., others, 2019a. Controllable organic magnetoresistance in polyaniline coated poly (p-phenylene-2, 6-benzobisoxazole) short fibers. Chem. Commun.

Gu, H., Xu, X., Dong, M., Xie, P., Shao, Q., Fan, R., Liu, C., Wu, S., Wei, R., Guo, Z., 2019b. Carbon nanospheres induced high negative permittivity in nanosilver-polydopamine metacomposites. Carbon N. Y. 147, 550–558.

Guo, Y., Ruan, K., Yang, X., Ma, T., Kong, J., Wu, N., Zhang, J., Gu, J., Guo, Z., 2019. Constructing fully carbon-based fillers with a hierarchical structure to fabricate highly thermally conductive polyimide nanocomposites. J. Mater. Chem. C 7, 7035–7044. https://doi.org/10.1039/c9tc01804b

Guo, Y., Xu, G., Yang, X., Ruan, K., Ma, T., Zhang, Q., Gu, J., Wu, Y., Liu, H., Guo, Z., 2018. Significantly enhanced and precisely modeled thermal conductivity in polyimide nanocomposites with chemically modified graphene via in situ polymerization and

electrospinning-hot press technology. J. Mater. Chem. C 6, 3004–3015.

Haider, A., Haider, S., Kang, I.K., 2018. A comprehensive review summarizing the effect of electrospinning parameters and potential applications of nanofibers in biomedical and biotechnology. Arab. J. Chem. 11, 1165–1188. https://doi.org/10.1016/j.arabjc.2015.11.015

He, Y., Chen, Q., Liu, H., Zhang, L., Wu, D., Lu, C., OuYang, W., Jiang, D., Wu, M., Zhang, J., others, 2019. Friction and Wear of MoO3/Graphene Oxide Modified Glass Fiber Reinforced Epoxy Nanocomposites. Macromol. Mater. Eng. 1900166.

Hotaling, N.A., Bharti, K., Kriel, H., Simon, C.G., 2015. DiameterJ: A validated open source nanofiber diameter measurement tool. Biomaterials 61, 327–38. https://doi.org/10.1016/j.biomaterials.2015.05.015

Huan, S., Liu, G., Cheng, W., Han, G., Bai, L., 2018. Electrospun poly (lactic acid)-based fibrous nanocomposite reinforced by cellulose nanocrystals: Impact of fiber uniaxial alignment on microstructure and mechanical properties. Biomacromolecules 19, 1037–1046.

Huang, J., Cao, Y., Shao, Q., Peng, X., Guo, Z., 2017. Magnetic nanocarbon adsorbents with enhanced hexavalent chromium removal: morphology dependence of fibrillar vs particulate structures. Ind. Eng. Chem. Res. 56, 10689–10701.

Jiang, D., Wang, Y., Li, B., Sun, C., Wu, Z., Yan, H., Xing, L., Qi, S., Li, Y., Liu, H., others, 2019. Flexible Sandwich Structural Strain Sensor Based on Silver Nanowires Decorated with Self-Healing Substrate. Macromol. Mater. Eng. 1900074.

Kuppan, P., Sethuraman, S., Krishnan, U.M., 2016. Interaction of human smooth muscle cells on random and aligned nanofibrous scaffolds of PHBV and PHBV-gelatin. Int. J. Polym. Mater. Polym. Biomater. 65. https://doi.org/10.1080/00914037.2016.1163562

La Mantia, F.P., Ceraulo, M., Mistretta, M.C., Botta, L., 2018. Effect of the elongational flow on morphology and properties of polypropylene/graphene nanoplatelets nanocomposites. Polym. Test. 71, 10–17. https://doi.org/10.1016/j.polymertesting.2018.08.016

Li, H., Huang, C., Jin, X., Ke, Q., 2018. An electrospun poly (e-caprolactone) nanocomposite fibrous mat with a high content of hydroxyapatite to promote cell infiltration. RSC Adv. 8, 25228–25235.

Li, S., Yang, P., Liu, X., Zhang, J., Liu, C., Xie, W., Wang, C., Guo, Z., 2019. Graphene Oxide Based Dopamine Mussel-like Cross-linked Polyethylene Imine Nanocomposite Coating with Enhanced Hexavalent Uranium Adsorption. J. Mater. Chem. A.

Li, T., Tian, L., Liao, S., Ding, X., Irvine, S.A., Ramakrishna, S., 2019. Fabrication, mechanical property and in vitro evaluation of poly (L-lactic acid-co-ε-caprolactone) core-shell nanofiber scaffold for tissue engineering. J. Mech. Behav. Biomed. Mater. 98, 48–57.

https://doi.org/10.1016/j.jmbbm.2019.06.003

Lin, B., Lin, Z., Chen, S., Yu, M., Li, W., Gao, Q., Dong, M., Shao, Q., Wu, S., Ding, T., others, 2019. Surface intercalated spherical MoS 2x Se 2 (1- x) nanocatalysts for highly efficient and durable hydrogen evolution reactions. Dalt. Trans.

Liu, M., Li, B., Zhou, H., Chen, C., Liu, Y., Liu, T., 2017. Extraordinary rate capability achieved by a 3D skeleton/skin carbon aerogel-polyaniline hybrid with vertically aligned pores. Chem. Commun. 53, 2810–2813.

Lu, C., Chen, P., Li, J., Zhang, Y., 2006. Computer simulation of electrospinning. Part I. Effect of solvent in electrospinning. Polymer (Guildf). 47, 915–921. https://doi.org/10.1016/j.polymer.2005.11.090

Luo, X., Pei, F., Wang, W., Qian, H., Miao, K.-K., Pan, Z., Chen, Y.-S., Feng, G.-D., 2018a. Microwave synthesis of hierarchical porous materials with various structures by controllable desilication and recrystallization. Microporous Mesoporous Mater. 262, 148–153.

Luo, X., Pan, Z., Pei, F., Jin, Z., Miao, K., Yang, P., Qian, H., Chen, Q., Feng, G., 2018b. In situ growth of hollow Cu2O spheres using anionic vesicles as soft templates. J. Ind. Eng. Chem. 59, 410–415.

Ma, L., Li, N., Wu, G., Song, G., Li, X., Han, P., Wang, G., Huang, Y., 2018. Interfacial enhancement of carbon fiber composites by growing TiO2 nanowires onto amine-based functionalized carbon fiber surface in supercritical water. Appl. Surf. Sci. 433, 560–567.

Ma, L., Zhu, Y., Feng, P., Song, G., Huang, Y., Liu, H., Zhang, J., Fan, J., Hou, H., Guo, Z., 2019a. Reinforcing carbon fiber epoxy composites with triazine derivatives functionalized graphene oxide modified sizing agent. Compos. Part B Eng. 176, 107078.

Ma, L., Zhu, Y., Wang, M., Yang, X., Song, G., Huang, Y., 2019b. Enhancing interfacial strength of epoxy resin composites via evolving hyperbranched amino-terminated POSS on carbon fiber surface. Compos. Sci. Technol. 170, 148–156.

Ma, R., Wang, Y., Qi, H., Shi, C., Wei, G., Xiao, L., Huang, Z., Liu, S., Yu, H., Teng, C., others, 2019. Nanocomposite sponges of sodium alginate/graphene oxide/polyvinyl alcohol as potential wound dressing: In vitro and in vivo evaluation. Compos. Part B Eng. 167, 396–405.

Ma, Y., Hou, C., Zhang, H., Zhang, Q., Liu, H., Wu, S., Guo, Z., 2019. Three-dimensional core-shell Fe3O4/Polyaniline coaxial heterogeneous nanonets: Preparation and high performance supercapacitor electrodes. Electrochim. Acta 315, 114–123.

Ma, Y., Ma, M., Yin, X., Shao, Q., Lu, N., Feng, Y., Lu, Y., Wujcik, E.K., Mai, X., Wang, C., others, 2018. Tuning polyaniline nanostructures via end group substitutions and their morphology dependent electrochemical performances. Polymer (Guildf). 156, 128–135.

Miculescu, F., Maidaniuc, A., Miculescu, M., Dan Batalu, N., ta lin Ciocoiu, R., Voicu, S. tefan I., Stan, G.E., Thakur, V.K., 2018. Synthesis and characterization of jellified composites from bovine bone-derived hydroxyapatite and starch as precursors for robocasting. ACS omega 3, 1338–1349.

Miculescu, F., Maidaniuc, A., Voicu, S.I., Thakur, V.K., Stan, G.E., Ciocan, L.T., 2017a. Progress in hydroxyapatite--starch based sustainable biomaterials for biomedical bone substitution applications. ACS Sustain. Chem. Eng. 5, 8491–8512.

Miculescu, F., Mocanu, A.-C., Dascualu, C.A., Maidaniuc, A., Batalu, D., Berbecaru, A., Voicu, S.I., Miculescu, M., Thakur, V.K., Ciocan, L.T., 2017b. Facile synthesis and characterization of hydroxyapatite particles for high value nanocomposites and biomaterials. Vacuum 146, 614–622.

Milazzo, M., Contessi Negrini, N., Scialla, S., Marelli, B., Farè, S., Danti, S., Buehler, M.J., 2019. Additive Manufacturing Approaches for Hydroxyapatite-Reinforced Composites. Adv. Funct. Mater. 1903055.

Ni, P., Bi, H., Zhao, G., Han, Y., Wickramaratne, M.N., Dai, H., Wang, X., 2019. Electrospun preparation and biological properties in vitro of polyvinyl alcohol/sodium alginate/nano-hydroxyapatite composite fiber membrane. Colloids Surfaces B Biointerfaces 173, 171–177.

Pan, D., Ge, S., Zhao, J., Tian, J., Shao, Q., Guo, L., Mai, X., Wu, T., Murugadoss, V., Liu, H., others, 2018. Synthesis and characterization of ZnNiIn layered double hydroxides derived mixed metal oxides with highly efficient photoelectrocatalytic activities. Ind. Eng. Chem. Res. 58, 836–848.

Panda, R.N., Hsieh, M.F., Chung, R.J., Chin, T.S., 2003. FTIR, XRD, SEM and solid state NMR investigations of carbonate-containing hydroxyapatite nano-particles synthesized by hydroxide-gel technique. J. Phys. Chem. Solids 64, 193–199. https://doi.org/10.1016/S0022-3697(02)00257-3

Pandele, A.M., Comanici, F.E., Carp, C.A., Miculescu, F., Voicu, S.I., Thakur, V.K., Serban, B.C., 2017. Synthesis and characterization of cellulose acetate-hydroxyapatite micro and nano composites membranes for water purification and biomedical applications. Vacuum 146, 599–605.

Qian, Y., Yuan, Y., Wang, H., Liu, H., Zhang, J., Shi, S., Guo, Z., Wang, N., 2018. Highly efficient uranium adsorption by salicylaldoxime/polydopamine graphene oxide nanocomposites. J. Mater. Chem. A 6, 24676–24685.

Ray, S.S., Chen, S.-S., Li, C.-W., Nguyen, N.C., Nguyen, H.T., 2016. A comprehensive review: electrospinning technique for fabrication and surface modification of membranes for water

treatment application. RSC Adv. 6, 85495–85514.

Reneker, D.H., Yarin, A.L., 2008. Electrospinning jets and polymer nanofibers. Polymer (Guildf). 49, 2387–2425. https://doi.org/10.1016/j.polymer.2008.02.002

Ribeiro Neto, W.A., Pereira, I.H.L., Ayres, E., De Paula, A.C.C., Averous, L., Góes, A.M., Oréfice, R.L., Suman Bretas, R.E., 2012. Influence of the microstructure and mechanical strength of nanofibers of biodegradable polymers with hydroxyapatite in stem cells growth. Electrospinning, characterization and cell viability. Polym. Degrad. Stab. 97, 2037–2051. https://doi.org/10.1016/j.polymdegradstab.2012.03.048

Rieger, K.A., Birch, N.P., Schiffman, J.D., 2013. Designing electrospun nanofiber mats to promote wound healing--a review. J. Mater. Chem. B 1, 4531–4541.

Scaffaro, R., Gulino, F.E., Lopresti, F., 2018. Structure-property relationship and controlled drug release from multiphasic electrospun carvacrol-embedded polylactic acid/polyethylene glycol and polylactic acid/polyethylene oxide nanofiber mats. J. Ind. Text. In press. https://doi.org/https://doi.org/10.1177/1528083718801359

Scaffaro, R., Lopresti, F., 2018a. Properties-morphology relationships in electrospun mats based on polylactic acid and graphene nanoplatelets. Compos. Part A Appl. Sci. Manuf. 108, 23–29. https://doi.org/10.1016/J.COMPOSITESA.2018.02.026

Scaffaro, R., Lopresti, F., 2018b. Processing, structure, property relationships and release kinetics of electrospun PLA/Carvacrol membranes. Eur. Polym. J. 100C, 165–171. https://doi.org/10.1016/j.eurpolymj.2018.01.035

Scaffaro, R, Lopresti, F., Botta, L., 2018. PLA based biocomposites reinforced with Posidonia oceanica leaves. Compos. Part B Eng. 139, 1–11. https://doi.org/10.1016/j.compositesb.2017.11.048

Scaffaro, R., Lopresti, F., Botta, L., 2017a. Preparation, characterization and hydrolytic degradation of PLA/PCL co-mingled nanofibrous mats prepared via dual-jet electrospinning. Eur. Polym. J. 96. https://doi.org/10.1016/j.eurpolymj.2017.09.016

Scaffaro, R., Lopresti, F., Botta, L., 2017b. Preparation, characterization and hydrolytic degradation of PLA/PCL co-mingled nanofibrous mats prepared via dual-jet electrospinning. Eur. Polym. J. 96, 266–277. https://doi.org/10.1016/j.eurpolymj.2017.09.016

Scaffaro, R., Lopresti, F., Botta, L., Maio, A., 2016. Mechanical behavior of Polylactic acid/Polycaprolactone porous layered functional composites. Compos. Part B Eng. 98, 70–77. https://doi.org/10.1016/j.compositesb.2016.05.023

Scaffaro, R., Lopresti, F., Maio, A., Botta, L., Rigogliuso, S., Ghersi, G., 2017c. Electrospun PCL/GO-g-PEG structures: Processing-morphology-properties relationships. Compos. Part A

Appl. Sci. Manuf. 92, 97–107. https://doi.org/10.1016/j.compositesa.2016.11.005

Scaffaro, R., Lopresti, F., Sutera, A., Botta, L., Fontana, R.M., Gallo, G., 2017d. Plasma modified PLA electrospun membranes for actinorhodin production intensification in Streptomyces coelicolor A3(2) immobilized-cell cultivations. Colloids Surfaces B Biointerfaces 157, 233–241. https://doi.org/10.1016/j.colsurfb.2017.05.060

Scaffaro, R., Maio, A., Lopresti, F., 2019. Effect of graphene and fabrication technique on the release kinetics of carvacrol from polylactic acid. Compos. Sci. Technol. 169, 60–69. https://doi.org/https://doi.org/10.1016/j.compscitech.2018.11.003

Scaffaro, R., Maio, A., Lopresti, F., Botta, L., 2017e. Nanocarbons in Electrospun Polymeric Nanomats for Tissue Engineering: A Review. Polymers (Basel). 9, 76. https://doi.org/10.3390/polym9020076

Scaffaro, R., Sutera, F., Lopresti, F., 2017f. Using Taguchi method for the optimization of processing variables to prepare porous scaffolds by combined melt mixing/particulate leaching. Mater. Des. 131. https://doi.org/10.1016/j.matdes.2017.06.025

Shi, Z., Jia, C., Wang, D., Deng, J., Xu, G., Wu, C., Dong, M., Guo, Z., 2019a. Synthesis and characterization of porous tree gum grafted copolymer derived from Prunus cerasifera gum polysaccharide. Int. J. Biol. Macromol. 133, 964–970.

Shi, Z., Xu, G., Deng, J., Dong, M., Murugadoss, V., Liu, C., Shao, Q., Wu, S., Guo, Z., 2019b. Structural characterization of lignin from D. sinicus by FTIR and NMR techniques. Green Chem. Lett. Rev. 12, 235–243.

Stoch, A., Jastrzkebski, W., Brożek, A., Stoch, J., Szaraniec, J., Trybalska, B., Kmita, G., 2000. FTIR absorption--reflection study of biomimetic growth of phosphates on titanium implants. J. Mol. Struct. 555, 375–382.

Sun, H., Yang, Z., Pu, Y., Dou, W., Wang, C., Wang, W., Hao, X., Chen, S., Shao, Q., Dong, M., others, 2019. Zinc oxide/vanadium pentoxide heterostructures with enhanced day-night antibacterial activities. J. Colloid Interface Sci. 547, 40–49.

Surucu, S., Masur, K., Sasmazel, H.T., Von Woedtke, T., Weltmann, K.D., 2016. Atmospheric plasma surface modifications of electrospun PCL/chitosan/PCL hybrid scaffolds by nozzle type plasma jets for usage of cell cultivation. Appl. Surf. Sci. 385, 400–409.

Tian, J., Shao, Q., Zhao, J., Pan, D., Dong, M., Jia, C., Ding, T., Wu, T., Guo, Z., 2019. Microwave solvothermal carboxymethyl chitosan templated synthesis of TiO2/ZrO2 composites toward enhanced photocatalytic degradation of Rhodamine B. J. Colloid Interface Sci. 541, 18–29.

Vitrano, I., Pavia, F.C., Conoscenti, G., Lombardo, M.E., La Carrubba, V., Brucato, V., 2018. Evaluation of Hydroxyapatite distribution in a Poly-L-Lactic Acid (PLLA) scaffolds via Micro

Computed Tomography ($μ$CT). Chem. Eng. Trans. 64, 193–198.

Wang, J., Yuan, B., Han, R.P.S., 2018. Modulus of elasticity of randomly and aligned polymeric scaffolds with fiber size dependency. J. Mech. Behav. Biomed. Mater. 77, 314–320. https://doi.org/10.1016/j.jmbbm.2017.09.016

Xu, G., Shi, Z., Zhao, Y., Deng, J., Dong, M., Liu, C., Murugadoss, V., Mai, X., Guo, Z., 2019. Structural characterization of lignin and its carbohydrate complexes isolated from bamboo (Dendrocalamus sinicus). Int. J. Biol. Macromol. 126, 376–384.

Yang, F., Murugan, R., Wang, S., Ramakrishna, S., 2005. Electrospinning of nano/micro scale poly(l-lactic acid) aligned fibers and their potential in neural tissue engineering. Biomaterials 26. https://doi.org/10.1016/j.biomaterials.2004.06.051

Yang, J., Yang, W., Wang, X., Dong, M., Liu, H., Wujcik, E.K., Shao, Q., Wu, S., Ding, T., Guo, Z., 2019. Synergistically Toughening Polyoxymethylene by Methyl Methacrylate--Butadiene--Styrene Copolymer and Thermoplastic Polyurethane. Macromol. Chem. Phys. 220, 1800567.

Yang, P., Yang, L., Gao, Q., Luo, Q., Zhao, X., Mai, X., Fu, Q., Dong, M., Wang, J., Hao, Y., others, 2019. Anchoring carbon nanotubes and post-hydroxylation treatment enhanced Ni nanofiber catalysts towards efficient hydrous hydrazine decomposition for effective hydrogen generation. Chem. Commun. 55, 9011–9014.

Yang, X., Li, Y., He, W., Huang, Q., Zhang, R., Feng, Q., 2018. Hydroxyapatite/collagen coating on PLGA electrospun fibers for osteogenic differentiation of bone marrow mesenchymal stem cells. J. Biomed. Mater. Res. Part A 106, 2863–2870.

You, Z.R., Hu, M.H., Tuan-Mu, H.Y., Hu, J.J., 2016. Fabrication of poly(glycerol sebacate) fibrous membranes by coaxial electrospinning: Influence of shell and core solutions. J. Mech. Behav. Biomed. Mater. 63, 220–231. https://doi.org/10.1016/j.jmbbm.2016.06.022

Zhang, C., Feng, F., Zhang, H., 2018. Emulsion electrospinning: Fundamentals, food applications and prospects. Trends Food Sci. Technol. 80, 175–186. https://doi.org/https://doi.org/10.1016/j.tifs.2018.08.005

Zhang, C., Wang, L., Zhai, T., Wang, X., Dan, Y., Turng, L., 2016. The surface grafting of graphene oxide with poly (ethylene glycol) as a reinforcement for poly (lactic acid) nanocomposite scaffolds for potential tissue engineering applications. J. Mech. Behav. Biomed. Mater. 53, 403–413. https://doi.org/10.1016/j.jmbbm.2015.08.043

Zhang, L., Yu, W., Han, C., Guo, J., Zhang, Q., Xie, H., Shao, Q., Sun, Z., Guo, Z., 2017. Large Scaled Synthesis of Heterostructured Electrospun TiO2/SnO2 Nanofibers with an Enhanced Photocatalytic Activity. J. Electrochem. Soc. 164, H651–H656.

Zhang, Z., Zhang, J., Li, S., Liu, J., Dong, M., Li, Y., Lu, N., Lei, S., Tang, J., Fan, J., others, 2019.

Effect of graphene liquid crystal on dielectric properties of polydimethylsiloxane nanocomposites. Compos. Part B Eng. 107338.

Zhou, C., Shi, Q., Guo, W., Terrell, L., Qureshi, A.T., Hayes, D.J., Wu, Q., 2013. Electrospun bio-nanocomposite scaffolds for bone tissue engineering by cellulose nanocrystals reinforcing maleic anhydride grafted PLA. ACS Appl. Mater. Interfaces 5, 3847–3854. https://doi.org/10.1021/am4005072

Zhu, G., Cui, X., Zhang, Y., Chen, S., Dong, M., Liu, H., Shao, Q., Ding, T., Wu, S., Guo, Z., 2019. Poly (vinyl butyral)/graphene oxide/poly (methylhydrosiloxane) nanocomposite coating for improved aluminum alloy anticorrosion. Polymer (Guildf). 172, 415–422.